Medical Image Segmentation by Partitioning Spatially Constrained Fuzzy Approximation Spaces

Shaswati Roy and Pradipta Maji

***Abstract*—Image segmentation is an important prerequisite step for any automatic clinical analysis technique. It assists in visualization of human tissues, as accurate delineation of medical images requires involvement of expert practitioners, which is also time consuming. In this background, the rough-fuzzy clustering algorithm provides an effective approach for image segmentation. It handles uncertainties arising due to overlapping classes and incompleteness in class definition by partitioning the fuzzy approximation spaces. However, the existing rough-fuzzy clustering algorithms do not consider the spatial distribution of the image. They depend only on the distribution of pixels to determine their class labels. In this regard, this article introduces a new algorithm, termed as spatially constrained rough-fuzzy c-means (sRFCM) for medical image segmentation. The proposed sRFCM algorithm combines wisely the merits of rough-fuzzy clustering and local neighborhood information. In the proposed algorithm, the labels of local neighbors influence in the determination of the label of center pixel. The effect of local neighbors acts as a regularizer. Moreover, the proposed sRFCM algorithm partitions each cluster in possibilistic lower approximation or core region and probabilistic boundary region. The cluster centroid depends on the core and boundary regions, weight parameter, and neighborhood regularizer. A novel segmentation validity index, termed as neighborhood Silhouette, is proposed to find out the optimum values of regularizer and weight parameter, controlling the performance of the sRFCM. The efficacy of the proposed sRFCM algorithm, as well as several existing segmentation algorithms, is demonstrated on four brain MR volume databases and one HEp-2 cell image data.**

***Index Terms*—Medical imaging, rough-fuzzy clustering, rough sets, segmentation, spatial information.**

I. Introduction

AN IMAGE contains a number of different regions which are homogeneous with respect to image intensities or its textural properties. Image segmentation is a process of delineating these multiple distinct regions of a given image. It acts as an important initial stage during the analysis of medical images. The quality of image segmentation reflects the success of different computer-aided diagnosis and therapies. Thresholding is simple but popular segmentation method. It partitions a scaler image by using one or more thresholds [1]. The local information or histogram-based techniques [2], [3] are popular in this approach, which work reasonably well for the images containing adjacent high contrast subregions. However, thresholding methods are sensitive to outliers and noise, since spatial information of an image is not considered in this approach.

The local intensity information is incorporated into thresholding framework by Li *et al.* [4] to address this problem, while connectivity is used by Lee *et al.* [5] to solve the problem. For delineation of simple, small structures, the region-growing approach [6]–[8] is generally used, which is a popular technique for segmentation of medical images. In order to reduce the noise sensitive problem of region-growing approach, Mangin *et al.* [9] proposed a homotopic region growing algorithm. It can preserve the topology between initial and extracted regions. Neural networks, in both supervised [10] and unsupervised fashion [2], [11], are also successfully applied in the domain of image segmentation [12]. The snake model [13] has been used for image segmentation. Specifically, implicit active contour or level-set-based models have become popular in image segmentation [14]. Among other techniques, different approaches, based on k-means [15], [16], wavelet transform [17], graph-cut [18], and self-organizing maps [19], are applied in segmentation of images into various structures.

In medical image analysis, images incur noise and other imaging artifacts, such as outliers, intensity inhomogeneity, partial volume effect, etc. In addition, low resolution of the images, imbalance in tissue classes, and overlapping characteristics of different tissue classes make the segmentation problem challenging. In medical image segmentation, uncertainty is also one of the important problems. Both imprecision in computations and vagueness in segment or partition definition are some of the sources of this uncertainty. In this background, fuzzy c-means (FCM) algorithm is effective to capture the uncertainty in image segmentation [10], [20], [21]. In this approach, the uncertainties emerging from cluster boundaries or overlapping partitions are efficiently handled by assigning memberships to each pixel. The memberships of each pixel are inversely proportional to the relative distance between cluster prototypes and the pixel. In order to model different classes for segmentation, another popular framework existing in the literature is the probabilistic model. It uses expectation–maximization algorithm and assigns class labels of the pixels in an image based on their probability values. The probability is calculated using the distribution of intensity values. For image segmentation, the mostly used model is finite Gaussian mixture (FGM) model [22], [23].

Manuscript received May 20, 2019; revised September 23, 2019 and December 13, 2019; accepted December 17, 2019. Date of publication January 13, 2020; date of current version May 4, 2020. *(Corresponding author: Pradipta Maji.)*

The authors are with the Biomedical Imaging and Bioinformatics Lab, Machine Intelligence Unit, Indian Statistical Institute, Kolkata 700108, India (e-mail: r.shaswati@gmail.com; pmaji@isical.ac.in).

Color versions of one or more of the figures in this article are available online at http://ieeexplore.ieee.org.

Digital Object Identifier 10.1109/TFUZZ.2020.2965896

1063-6706 © 2020 IEEE. Personal use is permitted, but republication/redistribution requires IEEE permission.
See https://www.ieee.org/publications/rights/index.html for more information.

Authorized licensed use limited to: Indian Statistical Institute Kolkata. Downloaded on May 08,2020 at 03:48:34 UTC from IEEE Xplore. Restrictions apply.

Although both FGM- and FCM-based algorithms can efficiently capture uncertainties arising due to overlapping classes, the probabilistic or fuzzy membership of each pixel, assigned by them, is affected by different imaging artifacts. In order to reduce the difficulty due to the probabilistic or fuzzy memberships, the concept of clustering in fuzzy approximation spaces, popularly known as rough-fuzzy clustering, is presented in [24]–[26]. Each cluster in the rough-fuzzy clustering algorithms is assumed to be composed of two regions, namely, core region or lower approximation and overlapping region or fuzzy boundary. The core region impacts on the overlapping characteristics of the final partition. The centroid of each cluster is calculated based on the weighted average of core region and overlapping boundary region. As a result, the rough-fuzzy clustering is able to compensate the effect of noise sensitivity of the FCM or FGM [24]. Moreover, it is able to locate a cluster of arbitrary shape [25]. The successful application of rough-fuzzy clustering in the domain of image segmentation [17], [24], [26] has shown its dominance over both FCM and FGM.

However, the FCM, FGM or rough-fuzzy clustering algorithm-based existing works do not consider spatial information for segmentation of images. In effect, they are very much sensitive to different imaging artifacts. In general, an image can be represented by a number of homogeneous regions and every homogeneous region consists of one or more connected regions of pixels with similar properties. Hence, the FGM model based probabilistic framework is integrated with the hidden Markov random field model in [27] to reduce the effect of outliers and noise. The spatial constraint has also been incorporated into the FCM framework [28]–[38] to minimize the impacts of noise and outliers. In [39], Tolias and Panas introduced a fuzzy rule-based neighborhood system to incorporate the spatial information, which post-processes the clustering results of FCM. Ahmed *et al*. [29] included spatial information into the standard FCM, called fuzzy c-means using spatial information (FCM_S), to reduce the intensity nonuniformity artifacts by allowing the labeling of a pixel to be influenced by the labels in its immediate neighborhood. Chen and Zhang [36] introduced two modifications of the FCM_S, namely, spatially constrained fuzzy c-means with mean (FCM_S1) and spatially constrained fuzzy c-means with median (FCM_S2), by including additional information, mean and median filtered images as the spatial information. Since these filtered images can be generated in advance, the execution time is reduced considerably. They also extended FCM_S, FCM_S1, and FCM_S2 to KFCM_S, KFCM_S1, and KFCM_S2, respectively, by kernel function substitution in order to disclose non-Euclidean structures inherent in image. In [32], the fast generalized FCM algorithm is introduced by modifying the FCM_S or its variants. It assigns different values of regularizer parameter to different neighbors, which can be obtained from local spatial gray-level relationships.

Krinidis and Chatzis [37] proposed an algorithm, namely, fuzzy local information c-means (FLICM), which includes a fuzzy factor into the classical FCM. This fuzzy factor is independent of using any regularization parameter. Gong *et al.* [31] improved the FLICM, in which the kernel method with non-Euclidean distance measure is used and a tradeoff weighted fuzzy factor is introduced to make it robust to the outliers and noise of the image. Liu and Pham [40] introduced spatial constraints into fuzzy hyperplane-based clustering algorithm, where cluster centers are represented by hyperplanes. They used T1-weighted and FLAIR sequence scans, coregistered to each other, for segmentation of brain soft tissues. Zhang *et al.* [30] combined FCM_S and Student's t-distribution with mean template to estimate the prior probability of belongingness of a pixel to a class. Wang and Bu [34] presented a segmentation method for images, integrating the FCM and spatial information, in which the image feature is represented using a similarity measure. Finally, the image segmentation is performed using the FCM algorithm, where the membership function depends on inter pixel correlation. Liew and Yan [38] also introduced an adaptive spatial FCM algorithm, in which a dissimilarity index is introduced. This index considers spatial interactions among voxels, which, in effect, reduces the impact of noise and ambiguity in classification. Wan *et al.* [41] proposed Bayesian nonlocal spatial information based FCM algorithm. In [42], the correlation between a pixel and its neighboring pixels is considered to modify the objective function of FCM, by adaptive weighting fusion of local mean information; while Zhang *et al.* [43] introduced sparsity and neighbor information constraint in the fuzzy clustering framework. Recently, deep learning models [44] have also been applied in the domain of medical image segmentation, due to their ability to provide high segmentation accuracy.

In this regard, this article introduces a novel rough-fuzzy clustering algorithm for image segmentation, named spatially constrained rough-fuzzy c-means (sRFCM). It judiciously incorporates neighborhood information of a pixel into existing robust rough-fuzzy c-means (rRFCM) [25]. It considers the spatial distribution of a pixel, and based on this neighboring information, it determines the class label of that pixel. In this way, it improves the quality of image segmentation. As a result, the sRFCM can avoid the problem of sensitivity to imaging artifacts of existing rough-fuzzy clustering algorithms. The relative importance of the regularization term controls the neighborhood effect. It also balances between reduction of noise and preserving the image details. Each cluster of the sRFCM algorithm consists of a core and a boundary regions. The boundary region is fuzzy, while the core region is possibilistic in nature. While the integration of both possibilistic as well as probabilistic membership functions of fuzzy sets handles efficiently overlapping segments in presence of noise, the vagueness, incompleteness, and uncertainty in the definition of a given class can be dealt by the concept of boundary region and lower approximation of rough sets. The class representative is determined by the weighted average of possibilistic core region and fuzzy overlapping region, as well as the neighborhood regularizer. A new quantitative index, termed as neighborhood Silhouette, is introduced to determine the optimal values of various parameters controlling the performance of the proposed sRFCM algorithm. The efficacy of the proposed sRFCM is demonstrated with respect to several existing related algorithms on a set of benchmark data sets both qualitatively and quantitatively.

Authorized licensed use limited to: Indian Statistical Institute Kolkata. Downloaded on May 08,2020 at 03:48:34 UTC from IEEE Xplore. Restrictions apply.

II. sRFCM: Spatially Constrained Rough-Fuzzy Clustering Algorithm

In this section, a new c-means algorithm, termed as sRFCM, is presented for delineation of different subregions of a given image. The proposed algorithm wisely includes the neighborhood information of pixels into existing rRFCM algorithm [25]. In the proposed algorithm, the class labels of the local neighboring pixels influence in the determination of the class label of center pixel. The effect of neighborhood plays the role of a regularizer and forces the labeling to be piecewise-homogeneous. This regularization has an important role in segmenting a noise-corrupted image. Moreover, the uncertainty and incompleteness in class definition is dealt using the core and boundary regions of rough sets of the proposed c-means algorithm, while overlapping clusters in noisy environment is effectively handled by the integration of both fuzzy and possibilistic memberships of fuzzy set.

A. Objective Function

Let $V = \{v_1, \ldots, v_i, \ldots, v_c\}$ be the set of c centroids, where $v_i \in \Re^m$ and $X = \{x_1, \ldots, x_j, \ldots, x_n\}$ be the set of n pixels, where $x_j \in \Re^m$. In the sRFCM, each segment or class β_i is represented by a class prototype or centroid v_i, a possibilistic core region $\underline{A}(\beta_i)$ and a fuzzy boundary $B(\beta_i)$. Let $\overline{A}(\beta_i)$ be the upper approximation of class β_i. Therefore, $B(\beta_i) = [\overline{A}(\beta_i) \setminus \underline{A}(\beta_i)]$. The objective function of the sRFCM algorithm can be computed separately for boundary region and lower approximation as follows:

$$J = \sum_{i=1}^{c} J_i; \quad \text{where } J_i = \omega J_i^L + (1-\omega) J_i^B. \tag{1}$$

Here, J_i^L and J_i^B are the objective functions for lower approximation and boundary region of cluster β_i, respectively, which are represented as follows:

$$J_i^L = \sum_{x_j \in \underline{A}(\beta_i)} \nu_{ij}^{\acute{m}_2} d_{ij}^2 + \eta_i \sum_{x_j \in \underline{A}(\beta_i)} (1-\nu_{ij})^{\acute{m}_2} + \frac{\alpha}{N_R} \sum_{x_j \in \underline{A}(\beta_i)} \nu_{ij}^{\acute{m}_2} \sum_{x_r \in \mathcal{N}_j} d_{ir}^2 \tag{2}$$

$$J_i^B = \sum_{x_j \in B(\beta_i)} \mu_{ij}^{\acute{m}_1} d_{ij}^2 + \frac{\alpha}{N_R} \sum_{x_j \in B(\beta_i)} \mu_{ij}^{\acute{m}_1} \sum_{x_r \in \mathcal{N}_j} d_{ir}^2 \tag{3}$$

where $d_{ij}^2 = ||x_j - v_i||^2$, μ_{ij} is the probabilistic or fuzzy membership function, and ν_{ij} represents the possibilistic membership function subject to the constraints given as follows:

$$\sum_{i=1}^{c} \mu_{ij} = 1, \forall j, \; 0 < \sum_{j=1}^{n} \mu_{ij} < n, \forall i \tag{4}$$

$$0 < \sum_{j=1}^{n} \nu_{ij} \leq n, \forall i; \text{ and } \max_i \nu_{ij} > 0, \forall j \tag{5}$$

and η_i is the scale parameter, which is given by

$$\eta_i = \mathrm{K} \cdot \left[\sum_{j=1}^{n} \nu_{ij}^{\acute{m}_2} d_{ij}^2 \right] \left[\sum_{j=1}^{n} \nu_{ij}^{\acute{m}_2} \right]^{-1} \tag{6}$$

which represents the size of β_i and is termed as zone of influence of β_i. Generally, K is considered to be 1. If the first and third terms of the criterion function for lower approximation, presented in (2), are only considered, without considering the second term, the function is minimized by assigning all memberships to 0, which is its trivial solution. However, according to the theory of rough sets, the memberships of the objects belonging to lower approximation of a cluster should be as high as possible. So, the second term of (2) forces the membership ν_{ij} to be as large as possible, thus avoiding the trivial solution.

The relative importance of core and boundary regions depends on the parameter ω, while the probabilistic and possibilistic fuzzifiers are represented by $\acute{m}_1 \in [1, \infty)$ and $\acute{m}_2 \in [1, \infty)$, respectively. Typically, $\acute{m}_1$ and $\acute{m}_2$ are considered to be 2.0. The term $\mathcal{N}_j$ is the set of neighboring pixels falling into a specified window $R \times R$ around x_j and N_R is the cardinality of $\mathcal{N}_j$. The parameter $\alpha \in [0, 1]$ controls the influence of the neighboring term. Hence, it balances between reduction of noise and preserving the image details. If the neighborhood window is in a homogeneous region with center pixel being noise, then the center pixel is smoothed by its neighboring pixels appropriately during membership and cluster prototype computation.

In accordance with the notion of rough sets, if a pixel x_j exists in the core region or lower approximation $\underline{A}(\beta_i)$ of a class or segment β_i, then x_j does not belong to the lower approximations or boundary regions of any other clusters. In other words, the pixel x_j belongs to the cluster or segment β_i definitely. Therefore, other centroids and clusters do not contribute in the calculation of the memberships of the pixels lying in core region of a cluster. In addition, different pixels of a core region may have different influences on the corresponding centroid and cluster according to their distances from the corresponding cluster prototype. On the other hand, a pixel x_j belonging to the boundary region $B(\beta_i)$ of segment β_i indicates that x_j possibly belongs to the segment β_i and potentially belongs to another cluster. So, the effect of the pixels present in boundary regions of different clusters is different in computation of these cluster centroids and the positions of all cluster centroids determine the memberships of the boundary region pixels. So, in the sRFCM, the membership values of pixels lying in core and boundary regions are similar to (7) of possibilistic c-means and (8) of FCM, respectively, excluding spatial constraints of the sRFCM.

B. Membership Functions

The possibilistic and probabilistic membership functions, namely, ν_{ij} and μ_{ij}, of a pixel x_j in cluster β_i can be derived by solving (2) and (3) with respect to ν_{ij} and μ_{ij}, respectively. Optimizing (2) with respect to ν_{ij}, we get

$$\nu_{ij} = \left[1 + \left\{ \frac{d_{ij}^2 + \frac{\alpha}{N_R} \sum_{x_r \in \mathcal{N}_j} d_{ir}^2}{\eta_i} \right\}^{\frac{1}{(\acute{m}_2 - 1)}} \right]^{-1}. \tag{7}$$

Authorized licensed use limited to: Indian Statistical Institute Kolkata. Downloaded on May 08,2020 at 03:48:34 UTC from IEEE Xplore. Restrictions apply.

Similarly, optimizing (3) with respect to μ_{ij}, given the constraint of (4), we get

$$\mu_{ij} = \left[\sum_{k=1}^{c} \left(\frac{d_{ij}^2 + \frac{\alpha}{N_R} \sum_{x_r \in \mathcal{N}_j} d_{ir}^2}{d_{kj}^2 + \frac{\alpha}{N_R} \sum_{x_r \in \mathcal{N}_j} d_{kr}^2} \right)^{\frac{1}{\acute{m}_1 - 1}} \right]^{-1}. \quad (8)$$

Combining (7) and (8), the following relation, between the probabilistic and possibilistic memberships of a pixel x_j in cluster β_i, can be established

$$\mu_{ij} = \left[\sum_{k=1}^{c} \left\{ \frac{\eta_i}{\eta_k} \left(\frac{\nu_{kj}(1-\nu_{ij})}{\nu_{ij}(1-\nu_{kj})} \right)^{\acute{m}_2 - 1} \right\}^{\frac{1}{\acute{m}_1 - 1}} \right]^{-1}. \quad (9)$$

Hence, it can be seen that for each pixel x_j of segment or cluster β_i, its probabilistic membership μ_{ij} is directly proportional to its possibilistic membership ν_{ij}.

C. Cluster Prototypes

The cluster prototype or centroid depends on both core and boundary regions of a cluster. The centroid of the proposed sRFCM algorithm is obtained by solving (1), (2), and (3) with respect to v_i as follows:

$$v_i = \omega v_i^L + (1-\omega) v_i^B, \quad i = 1, \ldots, c \quad (10)$$

$$\text{where } v_i^L = \frac{\sum_{x_j \in \underline{A}(\beta_i)} \nu_{ij}^{\acute{m}_2} \left(x_j + \frac{\alpha}{N_R} \sum_{x_r \in \mathcal{N}_j} x_r \right)}{(1+\alpha) \sum_{x_j \in \underline{A}(\beta_i)} \nu_{ij}^{\acute{m}_2}} \quad (11)$$

$$\text{and } v_i^B = \frac{\sum_{x_j \in B(\beta_i)} \mu_{ij}^{\acute{m}_1} \left(x_j + \frac{\alpha}{N_R} \sum_{x_r \in \mathcal{N}_j} x_r \right)}{(1+\alpha) \sum_{x_j \in B(\beta_i)} \mu_{ij}^{\acute{m}_1}}. \quad (12)$$

Hence, the cluster prototype depends on the characteristics of neighborhood pixels along with the center pixel, restricted by the parameter α. The value of ω rules the relative importance of pixels lying in core and boundary regions.

D. Computation of Thresholds

Similar to other rough-fuzzy clustering algorithms [24], [25], the proposed sRFCM algorithm partitions each cluster into two regions, namely, core and boundary regions by thresholding membership values of the pixels. Let us consider two thresholds δ_B and δ_L that represent the belongingness of the pixels in upper approximation and lower approximation of a given class, respectively. In other words, these two thresholds control the size of granules of the sRFCM algorithm. The threshold δ_L is defined as follows:

$$\delta_L = \frac{1}{n} \sum_{j=1}^{n} \left(\nu_{ij}^{(0)} - \nu_{kj}^{(0)} \right) \quad (13)$$

where $\nu_{ij}^{(0)}$ and $\nu_{kj}^{(0)}$ represent the highest and second highest possibilistic membership values of pixel x_j at iteration $t = 0$. The average of the differences between two initial highest membership values of each pixel in the image determines the value of δ_L. The value of δ_L should be as high as possible for a good segmentation algorithm. On the other hand, the pixels, those are not lying in the core region of any cluster, contribute to calculate the threshold δ_B

$$\delta_B = \frac{1}{\acute{n}} \sum_{j=1}^{\acute{n}} \nu_{ij}^{(0)} \quad (14)$$

where $\acute{n}$ represents the number of pixels with $(\nu_{ij}^{(0)} - \nu_{kj}^{(0)}) \leq \delta_L$ and $\nu_{ij}^{(0)}$ is the highest membership of pixel x_j.

E. Details of the Algorithm

The proposed sRFCM algorithm initially identifies c pixels as the c cluster prototypes. In order to compute the values of η_i for c clusters using (6), the possibilistic membership ν_{ij} of each pixel is calculated using (7). Next, the difference between two highest possibilistic memberships of each pixel x_j is computed. If the difference is greater than δ_L, then $x_j \in \underline{A}(\beta_i)$ and $x_j \in \overline{A}(\beta_i)$, based on the definition of rough sets. Otherwise, $x_j \in B(\beta_i)$ and $x_j \in B(\beta_k)$ if $\nu_{ij} > \delta_B$. In addition, x_j does not belong to core regions of any other clusters. Based on δ_L and δ_B, each pixel is assigned to core or boundary regions of different clusters. Next, the probabilistic memberships μ_{ij} for c clusters are computed from possibilistic memberships ν_{ij} using (9) for the pixels belonging to boundary regions of different clusters. The centroids of different clusters are then updated as per (10). The basic steps of the sRFCM algorithm proceed as follows.

1) Initialize different parameters of the algorithm, namely, $\acute{m}_1$, $\acute{m}_2$, ω, α, and N_R and c centroids $v_i, i = 1, \ldots, c$.
2) Compute the values of thresholds δ_L and δ_B using (13) and (14), respectively, and scale parameter η_i for cluster β_i by (6). Set iteration counter $t = 1$.
3) Calculate membership $\nu_{ij}^{(t)}$ for each pixel x_j and each cluster β_i using (7).
4) For each pixel x_j, find out highest and second highest possibilistic memberships, $\nu_{ij}^{(t)}$ and $\nu_{kj}^{(t)}$, respectively.
5) If $(\nu_{ij}^{(t)} - \nu_{kj}^{(t)}) > \delta_L$, then $x_j \in \underline{A}(\beta_i)$.
6) Otherwise, if $\nu_{ij}^{(t)} > \delta_B$, $x_j \in B(\beta_i)$ and $x_j \in B(\beta_k)$.
7) Compute $\mu_{ij}^{(t)}$ for all pixels x_j lying in boundary regions of different clusters using $\nu_{ij}^{(t)}$ by (9).
8) Calculate the new centroids using (10).
9) Steps 3–8 are repeated until maximum number of iterations is reached or no more new assignments can be made.
10) Stop.

F. Significance of Spatial Constraint

The noise sensitivity of the proposed sRFCM algorithm relies on the definition of spatial constraint introduced by the third and second terms of the objective functions of (2) and (3), respectively. The determination of this spatial constraint does not require any prior knowledge about the noise. Fig. 1 shows two basic cases that describe the performance of the proposed

Authorized licensed use limited to: Indian Statistical Institute Kolkata. Downloaded on May 08,2020 at 03:48:34 UTC from IEEE Xplore. Restrictions apply.

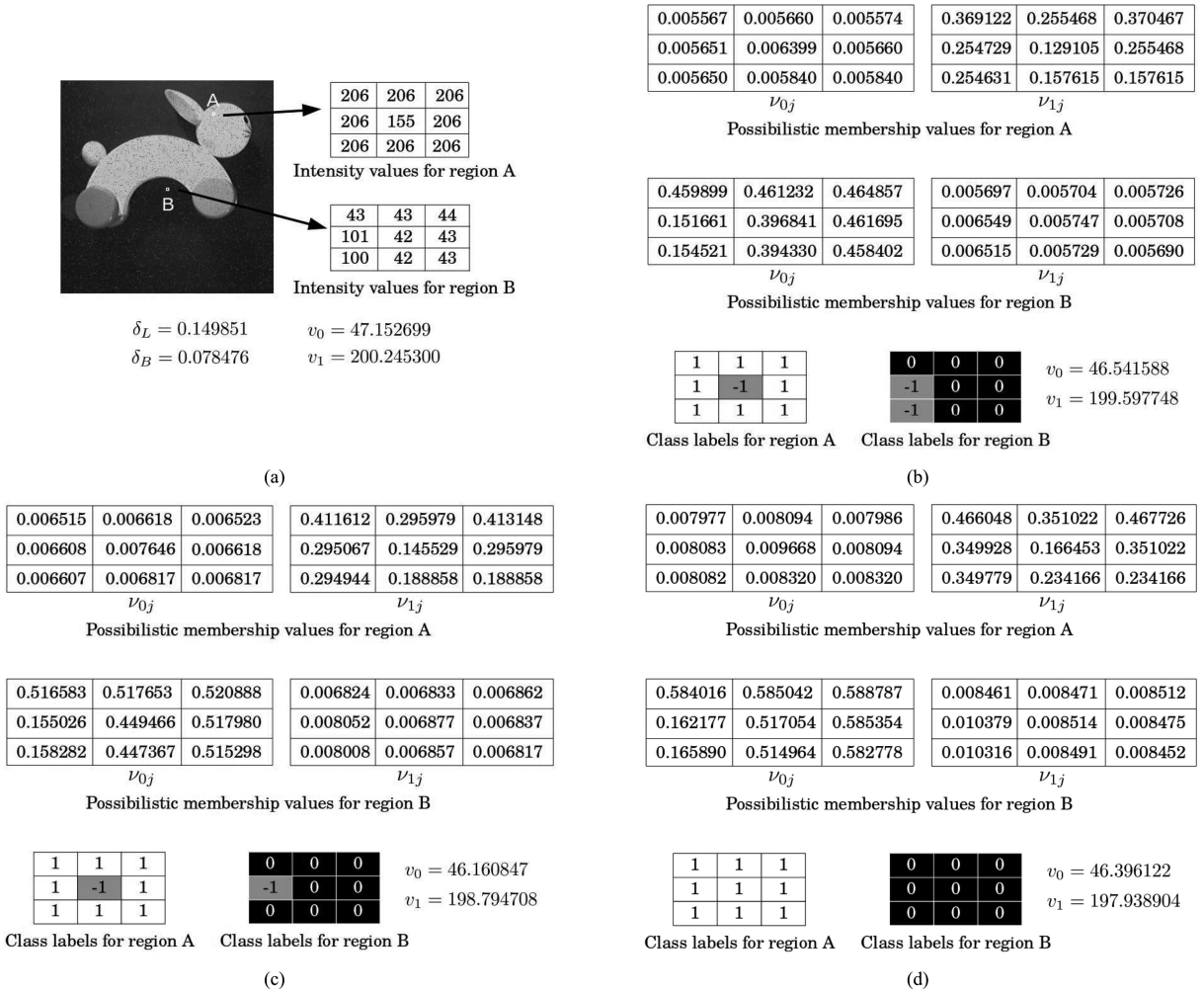

Fig. 1. Two 3×3 windows corrupted with noise (marked with rectangles in the input image), their corresponding possibilistic membership values, class labels, and cluster centroids (v_0 and v_1). (a) Input image with two selected regions, intensity values of the selected regions, and two thresholds δ_L and δ_B; and membership values, class labels, and centroids after (b) first iteration, (c) third iteration, and (d) fifth iteration.

sRFCM algorithm in presence of noise. Two 3×3 windows, marked as A and B in Fig. 1(a), are extracted from the input image to represent two different situations. The pixel intensity values for both regions A and B, the threshold values δ_L and δ_B computed using (13) and (14), respectively, and initial centroids of two classes, namely, background β_0 and object β_1, are also reported here. Fig. 1(b)–(d) present the possibilistic membership values and class labels of the pixels belonging to both regions A and B, and the centroids of β_0 and β_1, after different iterations.

1) *Case 1:* The center pixel of a local window, represented by A in Fig. 1(a), is corrupted by noise, while the other pixels within the window are homogeneous. Analyzing the examples shown in Fig. 1, it is seen that initially [Fig. 1(b)] as well as after third iteration [Fig. 1(c)] the noisy center pixel is lying in boundary region of β_1, since the difference between the possibilistic membership values of the center pixel for two classes is less than the threshold δ_L. Therefore, the class label of the center pixel of region A is -1, while that of other pixels within the window are assigned to the core region of β_1, denoted by 1. After fifth iteration, the difference between the possibilistic membership values of the noisy center pixel becomes higher than δ_L and its class label converges to the class labels of neighboring pixels, as shown in Fig. 1(d). Here, the spatial term balances the membership values of the center noisy pixel considering the information from its noise-free neighboring pixels. Thus, the influence of noise on the center pixel can be reduced by incorporating spatial constraints.
2) *Case 2:* The center pixel is not a noisy pixel and some pixels within its local window may be corrupted by noise, as shown in region B of Fig. 1(a). In Fig. 1(b), it is seen that after first iteration, the noisy pixels are assigned to the boundary region of β_0. After third iteration, one noisy pixel is assigned to same class label as that of neighboring pixels, as shown in Fig. 1(c). After fifth iteration, the algorithm converges for region B and the corresponding class labels of the noisy as well as that of the nonnoisy pixels converge to the same label as depicted in Fig. 1(d), ignoring the impact of the noisy pixels.

Therefore, the spatial constraints incorporated in the objective functions of (2) and (3) suppress the influence of the noisy

Authorized licensed use limited to: Indian Statistical Institute Kolkata. Downloaded on May 08,2020 at 03:48:34 UTC from IEEE Xplore. Restrictions apply.

pixels, and hence, the proposed algorithm becomes more robust to noise.

G. Convergence Criterion

A mathematical analysis is presented in this section on the convergence property of the proposed sRFCM algorithm. In accordance with (10), each cluster representative of the sRFCM method is determined from the weighted average of possibilistic core region and probabilistic or fuzzy boundary. Hence, the convergence of v_i depends on the convergence of v_i^L and v_i^B. Both (11) and (12) can be rewritten as

$$(|\underline{A}(\beta_i)|)v_i^L = \sum_{x_j \in \underline{A}(\beta_i)} \nu_{ij}^{\acute{m}_2} \left(x_j + \frac{\alpha}{N_R} \sum_{x_r \in \mathcal{N}_j} x_r \right) \quad (15)$$

$$(|B(\beta_i)|)v_i^B = \sum_{x_j \in B(\beta_i)} \mu_{ij}^{\acute{m}_1} \left(x_j + \frac{\alpha}{N_R} \sum_{x_r \in \mathcal{N}_j} x_r \right) \quad (16)$$

$$\text{where } |\underline{A}(\beta_i)| = (1+\alpha) \sum_{x_j \in \underline{A}(\beta_i)} \nu_{ij}^{\acute{m}_2} \quad (17)$$

$$\text{and } |B(\beta_i)| = (1+\alpha) \sum_{x_j \in B(\beta_i)} \mu_{ij}^{\acute{m}_1} \quad (18)$$

represent, respectively, the cardinality of core and boundary regions of cluster β_i. If both μ_{ij} and ν_{ij} are kept constant, both (15) and (16) represent a set of linear equations in terms of v_i^L and v_i^B. According to the analysis reported in [24], both (11) and (12) can be viewed as Gauss–Seidel iterations for solving the set of linear equations. Since the matrix representing each equation is diagonally dominant, that is

$$(1+\alpha) \sum_{x_j \in \underline{A}(\beta_i)} \nu_{ij}^{\acute{m}_2} > 0; \quad (1+\alpha) \sum_{x_j \in B(\beta_i)} \mu_{ij}^{\acute{m}_1} > 0 \quad (19)$$

the convergence of the proposed sRFCM algorithm is guaranteed [45]. If (11) and (12) were applied repetitively keeping the values of μ_{ij} and ν_{ij} fixed, the iteration would converge under the condition (19). In practice, (7), (8), and (10) are applied alternatively in the iterations. According to convergence theorem of fuzzy clustering derived by Bezdek [46] and the convergence analysis of rough-fuzzy clustering algorithm reported in [24], the condition of (19) is still correct. Hence, it can be concluded that as long as the condition in (19) is satisfied, the proposed algorithm converges, at least, to a local optimum solution.

H. Selection of Optimum Parameters

The parameter ω represents the relative importance of core region with respect to the boundary region of a given cluster. So, it influences directly the overall performance of the sRFCM algorithm. Since the pixels present in core region definitely belong to that cluster, it is desirable to give them more weightage compared to the pixels lying in boundary region. However, when $\omega \simeq 1.0$, clusters cannot see the boundary region pixels, thereby, reduces the mobility of the centroids and the clusters. In effect, a number of centroids may get stuck in local optimum. Therefore, $0 < 1 - \omega < \omega < 1.0$ is a good choice to have the clusters with a greater degree of freedom to move. On the other hand, the parameter α affects the smoothness of segmentation results. It controls the incorporation of spatial information in the clustering algorithm. If $\alpha = 0.0$, it does not consider the neighborhood details at all, and the proposed sRFCM boils down to the rRFCM [25]. When the value of α is very small, the sRFCM algorithm does not work well in noisy environment. On the other hand, detailed information is lost for a large value of α. In other words, the value of α has to be chosen large enough to tolerate the noise, while it has to be chosen small enough to preserve the image sharpness and details. Hence, the selection of appropriate value of α is crucial in order to achieve robust segmentation.

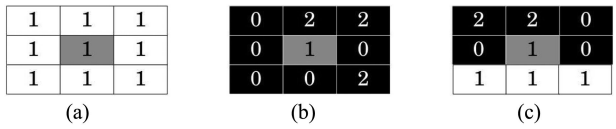

Fig. 2. Illustration of three cases of neighborhood Silhouette $\theta(i)$. (a) $\theta(i) = 1$. (b) $\theta(i) = -1$. (c) $\theta(i) = \Delta(i)$.

Neighborhood Silhouette: In general, an image can be considered as a collection of nonoverlapping, consistent regions, which are homogeneous with respect to some characteristics such as intensity values or textures. Hence, a cluster validity index, which includes the spatial information in computation, may be the appropriate choice for determining optimum parameter set for image segmentation. In this regard, a segmentation validity index, termed as neighborhood Silhouette, is proposed to find out the optimum values of ω and α.

For computing the neighborhood Silhouette $\theta(i)$ of a pixel or a point x_i, a neighborhood $\mathcal{N}_i$ of x_i is considered, instead of considering all pixels of the given image. Let β_r be the class or segment to which the pixel x_i belongs to. If a pixel x_i belongs to a cluster to which all of its neighbors belong to, then its neighborhood Silhouette is 1 [Fig. 2(a)]. On the other hand, the neighborhood Silhouette of the pixel x_i is -1 if it belongs to the cluster to which none of its neighbors belongs to [Fig. 2(b)]. If some of the neighbors, but not all, have the same class label as that of the center pixel x_i [Fig. 2(c)], then two scalar values $b(i)$ and $a(i)$ are computed for the pixel x_i within the neighborhood $\mathcal{N}_i$. The term $a(i)$ is estimated as the average of the distances of x_i and $x_j \in \mathcal{N}_i$ that belongs to the same class β_r. For any other class $\beta_s, s \neq r = 1, \ldots, c$, let $d(x_i, \beta_s)$ be the average of the distances between the pixel x_i to all pixels of β_s within the given neighborhood. The term $b(i)$ is the minimum of these computed distances $d(x_i, \beta_s)$. In this case, the neighborhood Silhouette of x_i is defined as

$$\Delta(i) = \frac{b(i) - a(i)}{\max\{a(i), b(i)\}}. \quad (20)$$

So, in brief, neighborhood Silhouette $\theta(i)$ of x_i is given by

$$\theta(i) = \begin{cases} -1, & \text{if } \forall x_j \notin \beta_r \\ 1, & \text{if } \forall x_j \in \beta_r \\ \Delta(i), & \text{otherwise} \end{cases} \quad (21)$$

where $x_j \in \mathcal{N}_i$ and β_r is the class label of center pixel x_i. So, the value of neighborhood Silhouette lies between -1 and 1.

Authorized licensed use limited to: Indian Statistical Institute Kolkata. Downloaded on May 08,2020 at 03:48:34 UTC from IEEE Xplore. Restrictions apply.

The global neighborhood Silhouette is then defined as follows:

$$\Theta = \frac{1}{c}\sum_{r=1}^{c}\frac{1}{|\beta_r|}\sum_{x_i\in\beta_r}\theta(i). \tag{22}$$

The compactness of the segmented regions is ensured by the higher value of Θ, which represents the importance of segmentation algorithm. Let $\mathcal{S} = \{\alpha, \omega\}$ be the set of parameters, while $\mathcal{S}^\star = \{\alpha^\star, \omega^\star\}$ be the set of optimal parameters. In order to obtain the values of $\alpha^\star$ and $\omega^\star$ for an input image, the proposed index Θ, that is, neighborhood Silhouette, is used. For a given image, the values of parameters ω and α are varied within a certain range. For each input image, the optimal values of these two parameters α and ω are found out by using the following relation:

$$\mathcal{S}^\star = \arg\max_{\mathcal{S}}\{\Theta\}. \tag{23}$$

III. Performance Analysis and Discussions

In this section, the performance of the proposed sRFCM algorithm is extensively studied with respect to different segmentation algorithms. The algorithms compared are Otsu thresholding [3], FCM_S [29], FCM_S1, and FCM_S2 filtering [36], kernelized versions of FCM_S (KFCM_S), FCM_S1 (KFCM_S1), and FCM_S2 (KFCM_S2) [36], FLICM [37], kernelized version of FLICM (KWFLICM) [31], and Gaussian distribution and hidden Markov random field (GHMRF) model [27]. Three analysis tools for MRI, namely, volBrain [47], FMRIB Software Library (FSL) version 4.1.9 [48], and statistical parameter mapping (SPM) version 8 [49], are also used for comparison. The source code of the proposed sRFCM algorithm, written in C language, is available online[1]. To study the comparative performance analysis of different algorithms and tools, three quantitative indices, namely, Dice coefficient, sensitivity, and specificity, and two cluster validity indices, namely, Davies–Bouldin (DB) and Dunn, are used.

The performance of different algorithms is analyzed on following five image databases: 1) MIVIA HEp-2 Images Dataset: It contains 28 HEp-2 cell images [50]; 2) BrainWeb (Subject): It contains twenty simulated normal brain MR volumes [51]; 3) BrainWeb (Noise-Bias): It consists of 18 simulated brain MR volumes corrupted with different levels of noise and bias [52]; 4) IBSR-18: It contains 18 real brain MR volumes and is available at Internet Brain Segmentation Repository (www.cma.mgh.harvard.edu/ibsr/); and 5) LPBA40: It consists of 40 real brain MR volumes [53]. Each brain MR volume is segmented into three regions, namely, gray matter (GM), white matter (WM), and cerebro-spinal fluid (CSF). Before applying any segmentation algorithm on brain MR volumes, the brain extraction tool with robust brain center estimation (version 2.1) [54] is applied to extract the brain tissues such as GM, WM, and CSF, while the intensity inhomogeneity artifact present in MR volumes is removed using N4ITK [55]. The Otsu thresholding method [3] is applied to achieve initial segmentation of HEp-2 cell images, while hard c-means algorithm is applied to estimate initial delineation of different tissue classes for brain MR volumes. The intensity value of a pixel is considered as its feature.

[1]1[Online]. Available: www.isical.ac.in/∼bibl/results/srfcm/srfcm.html

A. Determination of Optimum Parameters

This section presents the impact of different parameters on the performance of the proposed segmentation algorithm.

1) Optimum Values of ω and α: The performance of the proposed sRFCM algorithm mainly depends on two parameters, namely, weight parameter ω and neighborhood regularizer α. For each image, the optimum values of ω and α are determined using (23). The values of ω and α are varied from 0.51 to 0.99 and from 0.1 to 1.0, respectively. The size of neighborhood window R is considered as 3. Fig. 3(a) and (b) presents the variation of Dice coefficient and neighborhood Silhouette Θ with respect to ω considering corresponding $\alpha^\star$ value and that with respect to α for corresponding $\omega^\star$. Results are reported for the proposed sRFCM algorithm on two images as examples. From all the results reported in Fig. 3(a) and (b), it can be seen that the value of Dice coefficient varies according to that of the neighborhood Silhouette Θ as the parameters ω and α increase. Also, the highest value of Θ ensures higher value of Dice coefficient, in turn, better segmentation results.

In order to establish the correspondence between neighborhood Silhouette Θ of (22) and the compactness of the segmented region in terms of Dice coefficient, the correlation between Θ and Dice is computed for each image, considering 110 possible pairs of ω and α. The mean and standard deviation of correlation coefficient are then calculated, considering all images of a given data set. The mean values of correlation are 0.998839, 0.990731, 0.907702, 0.893168, and 0.890767 for BrainWeb (Noise-Bias), BrainWeb (Subject), IBSR-18, LPBA40, and HEp-2 Cell databases, respectively, while standard deviations are 0.000696, 0.018373, 0.086022, 0.056486, and 0.087922, respectively. From the results reported here, it is seen that the mean values of correlation coefficient are high, while the standard deviations are low, irrespective of the data sets used. It, thus, establishes that the neighborhood Silhouette corresponds to the compactness of the segmented region. Hence, the proposed parameter optimization method, based on the concept of neighborhood Silhouette, is effective in determining optimal values of parameters ω and α, irrespective of data sets used.

2) Importance of Higher Weight Value: In order to find out the optimum weight $\omega^\star$, the value of ω is varied in the range of 0.51–0.99. To establish the importance of higher value of ω, extensive experiment is carried out on five data sets considering $\omega \in (0.00, 0.50]$, and the best Dice coefficient obtained for this range of ω is compared with that achieved using the proposed parameter optimization technique where $\omega > 0.50$. Fig. 3(c) compares the performance of the proposed sRFCM algorithm when optimal $\omega^\star > 0.50$ is selected using (23) with that of the best performance in the range of 0.05 to 0.50. From all the results reported in Fig. 3(c), it is seen that the proposed sRFCM algorithm attains significantly better Dice coefficient when $\omega > 0.50$. In fact, higher weightage to the pixels belonging to core region, compared to those lying in boundary region,

Authorized licensed use limited to: Indian Statistical Institute Kolkata. Downloaded on May 08,2020 at 03:48:34 UTC from IEEE Xplore. Restrictions apply.

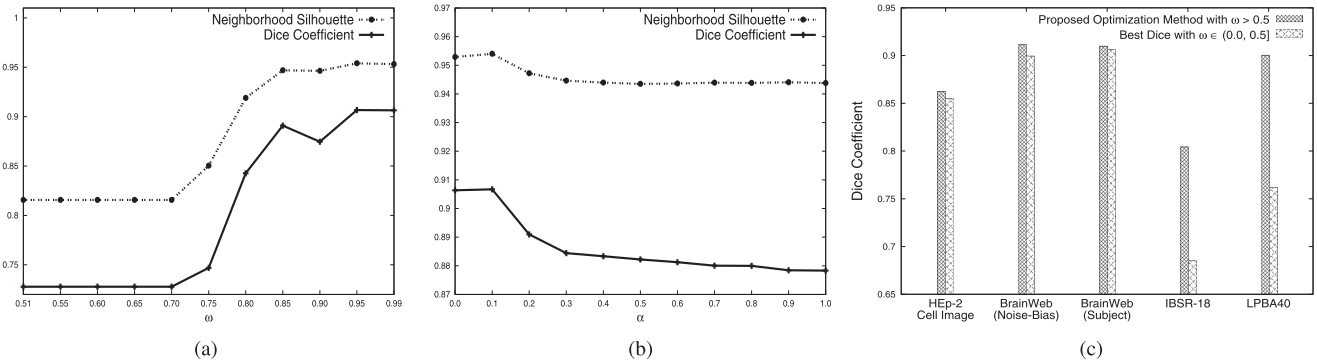

Fig. 3. Variation of Dice coefficient and neighborhood Silhouette for different values of (a) ω and (b) α; and (c) performance of the proposed algorithm with lower and higher ω values. (a) $\alpha^\star = 0.10$. (b) $\omega^\star = 0.95$. (c) Importance of higher ω.

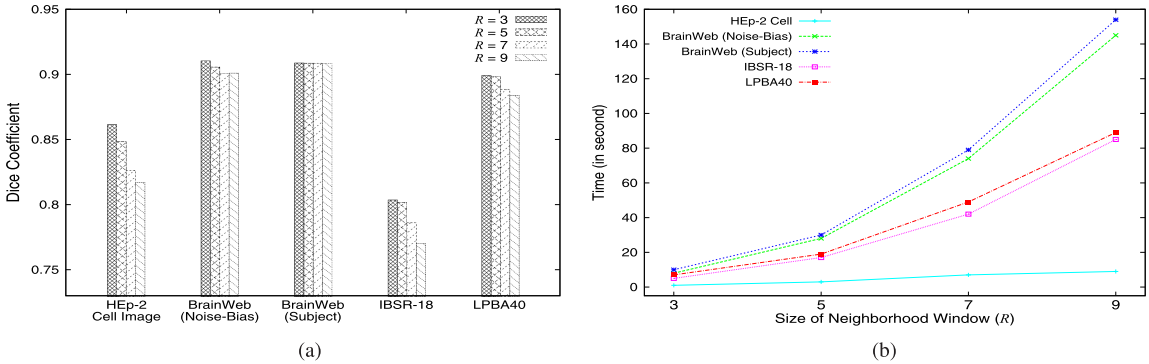

Fig. 4. Performance of the proposed algorithm for different sizes of neighborhood window in the computation of neighborhood Silhouette. (a) Segmentation accuracy. (b) Execution time.

helps to increase the performance drastically as the pixels of core region definitely belong to a cluster.

3) Optimum Window Size for Neighborhood Silhouette: The value of neighborhood Silhouette of (22) depends on the size of neighborhood window R. The larger size of window implies more number of pixels are considered for the computation of neighborhood Silhouette. Therefore, the value of neighborhood Silhouette changes with the change in neighborhood window. In effect, the optimal set of parameters obtained using (23) and corresponding segmentation performance of the proposed sRFCM algorithm depend on the size of window. Fig. 4 presents the performance of the proposed algorithm for different values of neighborhood window size R. The value of R is varied from 3 to 9 with a gap of 2. From the results reported in Fig. 4(a), it is seen that the sRFCM yields higher Dice coefficient when the neighborhood Silhouette is computed considering window size $R = 3$, irrespective of the data sets used. This is due to the fact that each brain MR volume contains a narrow region for CSF. As the dimension of neighborhood window increases, more number of voxels from different adjacent regions, mainly from GM, are included in neighborhood window. Although the voxels of CSF region are correctly classified by the proposed sRFCM algorithm, the values of neighborhood Silhouette for those voxels become very small due to the large neighborhood window.

Fig. 4(b) depicts the execution time required to compute neighborhood Silhouette, for different values of R. From the results reported in Fig. 4(b), it can be seen that the increase in neighborhood window drastically increases the computation time for brain MR volume data sets. This is because the number of voxels ($N_R = R^3 - 1$) in neighborhood window for different values of $R = 3, 5, 7,$ and 9 are $N_R = 26, 124, 342,$ and 728, respectively, for brain MR data, while the number of pixels ($N_R = R^2 - 1$) for HEp-2 cell image data set are $N_R = 8, 24, 48,$ and 80, respectively. Hence, although the proposed algorithm provides comparable segmentation performance for larger window size in case of BrainWeb (Noise-Bias), BrainWeb (Subject), and LPBA40 data sets, as reported in Fig. 4(a), smaller window size is desirable as it needs lesser time, as shown in Fig. 4(b). Therefore, in the current experiment, the size of neighborhood window is considered to be 3 for the computation of neighborhood Silhouette, to achieve better segmentation accuracy with significantly lesser time.

B. Importance of Spatial Constraints

It is seen that the existing rough-fuzzy clustering algorithms yield significantly more accurate results than fuzzy clustering algorithms in the domain of image segmentation [17], [24], [26]. However, they do not consider spatial information of pixels for segmentation. In effect, they are very much sensitive to different imaging artifacts. To address the shortcoming of existing rough-fuzzy clustering, the proposed sRFCM algorithm judiciously incorporates spatial constraints into rough-fuzzy

Authorized licensed use limited to: Indian Statistical Institute Kolkata. Downloaded on May 08,2020 at 03:48:34 UTC from IEEE Xplore. Restrictions apply.

clustering framework for image segmentation. In order to establish the advantage of spatial information included in rough-fuzzy clustering algorithm for segmentation, analysis is done on several HEp-2 cell images. From the experiments performed on 28 HEp-2 cell images obtained from MIVIA data set, it is seen that the sRFCM provides mean values of DB and Dunn indices as 4.148 and 0.381, respectively, while rRFCM attains the mean values 4.269 and 0.366, respectively. Also, the mean values of Dice coefficient, sensitivity, and specificity for the rRFCM are 0.842067, 0.830474, and 0.865255, respectively, while that of the sRFCM algorithm are 0.861453, 0.859821, and 0.866562, respectively. The comparative performance analysis is also done using Wilcoxon signed-rank test (one-tailed). The proposed sRFCM algorithm attains lower p-values of 3.86E-02, 1.72E-03, 2.08E-05, and 1.32E-03, respectively, with respect to the rRFCM algorithm for DB index, Dunn index, Dice coefficient, and sensitivity, which are statistically significant at 95% confidence level. However, the rRFCM attains lower, but not significant, p-value with respect to the sRFCM algorithm for specificity.

The importance of the proposed sRFCM algorithm in segmentation of brain MR volumes is also extensively studied and the performance of the sRFCM is compared with that of the rRFCM algorithm for four databases. For BrainWeb (Noise-Bias) database of 18 T1-weighted simulated brain MR volumes, the mean values of DB, Dunn, Dice coefficient, sensitivity, and specificity for the rRFCM algorithm are 0.127, 6.511, 0.896133, 0.880932, and 0.979409, respectively, while that of the sRFCM algorithm are 0.143, 7.109, 0.910208, 0.892975, and 0.981117, respectively. Also, the sRFCM achieves statistically significant p-values of 9.91E-03, 2.14E-02, 3.21E-02, and 8.81E-03, respectively, for Dunn, Dice, sensitivity, and specificity. Similarly, for BrainWeb (Subject) database of 20 simulated brain MR volumes, the mean values of DB index are 0.120 and 0.115, that of Dunn are 3.667 and 4.206, that of Dice coefficient are 0.907738 and 0.908544, that of sensitivity are 0.904775 and 0.904760, and that of specificity are 0.988387 and 0.988457, for rRFCM and sRFCM algorithms, respectively. In effect, the sRFCM attains significant p-values of 1.67E-02, 4.43E-05, and 6.02E-05 for Dunn, Dice, and specificity, respectively.

For real brain MR volumes of IBSR-18 and LPBA40 databases, the sRFCM algorithm achieves the mean values of DB index as 0.174 and 0.682, that of Dunn as 7.946 and 3.648, that of Dice coefficient as 0.803851 and 0.898982, that of sensitivity as 0.833570 and 0.924129, and that of specificity as 0.983470 and 0.992042, respectively. On the other hand, the rRFCM attains the mean values of DB index as 0.347 and 0.705, that of Dunn as 4.147 and 3.607, that of Dice as 0.778547 and 0.888276, that of sensitivity as 0.813987 and 0.917320, and that of specificity as 0.982291 and 0.991254, respectively. In effect, the sRFCM algorithm achieves statistically significant lower p-values of 2.68E-04, 9.82E-05, 9.82E-05, 7.96E-04, and 9.82E-05 for DB, Dunn, Dice, sensitivity, and specificity, respectively, on IBSR-18 database with respect to the rRFCM algorithm, while that of 2.49E-07, 7.92E-04, and 5.11E-08, for Dice, sensitivity, and specificity, respectively, on LPBA40 database. The sRFCM also attains lower p-values of 0.1099 and 0.0567 for DB and Dunn indices, which are not statistically significant. From all the results corresponding to five image databases, it can be seen that the incorporation of spatial information into rough-fuzzy clustering algorithm leads to significant improvement in segmentation performance from the existing rRFCM to the proposed sRFCM algorithm.

C. Performance of Different Segmentation Algorithms

In this section, the comparative performance analysis of the sRFCM algorithm and several existing segmentation algorithms on five databases is presented. The performance analysis of different methods is studied using tables of means, standard deviations, and p-values computed through Wilcoxon signed-rank test (one-tailed) with different segmentation metrics and cluster validity indices. Tables I, II, and III display the means and standard deviations of each of the five different metrics for all the methods, along with the p-values, computed through the sign test, with respect to the proposed method for five different data sets. The best mean values are marked as bold in these tables.

Tables I and II compare the performance of different segmentation algorithms with respect to two cluster validity indices. In case of HEp-2 MIVIA data set, the sRFCM algorithm achieves significantly lower DB and higher Dunn indices. Out of total 8 comparisons, the proposed algorithm attains significantly lower p-values in seven cases, and lower but not significant in 1 case, for both DB and Dunn indices. On the other hand, for brain MR tissue segmentation, the sRFCM obtains significantly lower p-values with respect to DB index in 31 cases, out of total 36 cases, and lower but not significant p-values in five cases. Analyzing the results in terms of Dunn index, it is seen that the sRFCM performs significantly better compared to all other methods for four brain MR data sets. Table I also highlights the improvement of performance of the proposed algorithm from initial segmentation by Otsu method for HEp-2 MIVIA data set. Analyzing the results depicted in Table I, it can be seen that the performance of the sRFCM is increased by 13.33%, 26.22%, 6.33%, and 3.88% with respect to Dice, sensitivity, DB, and Dunn indices, respectively.

Tables I, II, and III also compare the performance of different segmentation algorithms with respect to three segmentation indices. All the results reported here confirm that the proposed method attains best mean Dice coefficient and performs significantly better than any other algorithm at 95% confidence level, irrespective of the data sets used (marked in bold). Only for BrainWeb (Noise-Bias) and IBSR-18 databases, the sRFCM performs better than volBrain, but not significantly (marked in italics in Table III). The proposed method achieves significantly better results than all the existing algorithms with respect to sensitivity for HEp-2 MIVIA data set. Out of total 48 comparisons of four brain MR volume databases, the sRFCM algorithm attains significantly better results with respect to sensitivity in 32 cases and better but not significant in six cases compared to existing methods. On the other hand, the proposed method achieves significantly better results with respect to specificity in 42 cases and better but not significant in four cases for brain MR volume databases.

Authorized licensed use limited to: Indian Statistical Institute Kolkata. Downloaded on May 08,2020 at 03:48:34 UTC from IEEE Xplore. Restrictions apply.

TABLE I
COMPARATIVE PERFORMANCE ANALYSIS OF DIFFERENT ALGORITHMS ON HEP-2 CELL IMAGES

Different Algorithms	Davies-Bouldin Index			Dunn Index			Dice Coefficient			Sensitivity			Specificity		
	Mean	Std Dev	p-value	Mean	Std Dev	p-value	Mean	Std Dev	p-value	Mean	Std Dev	p-value	Mean	Std Dev	p-value
Otsu	4.429	3.432	**1.90E-6**	0.367	0.150	**1.90E-6**	0.760	0.155	**2.63E-6**	0.681	0.211	**1.89E-6**	0.939	0.069	1.00
FCM_S	4.436	3.497	**2.36E-6**	0.369	0.151	**2.63E-6**	0.773	0.143	**1.26E-5**	0.697	0.201	**5.54E-6**	0.939	0.062	1.00
FCM_S1	4.421	3.472	**2.36E-6**	0.370	0.151	**2.36E-6**	0.773	0.144	**1.03E-5**	0.696	0.201	**5.54E-6**	0.939	0.062	1.00
FCM_S2	4.411	3.457	**2.36E-6**	0.370	0.151	**2.63E-6**	0.771	0.146	**1.03E-5**	0.694	0.204	**6.15E-6**	0.939	0.064	1.00
KFCM_S	4.548	3.695	**2.36E-6**	0.366	0.151	**2.36E-6**	0.774	0.141	**6.83E-6**	0.700	0.199	**5.54E-6**	0.935	0.068	1.00
KFCM_S1	4.453	3.467	**2.63E-6**	0.366	0.149	**2.63E-6**	0.775	0.139	**6.83E-6**	0.700	0.198	**5.54E-6**	0.935	0.068	1.00
KFCM_S2	4.445	3.454	**2.36E-6**	0.366	0.149	**2.36E-6**	0.779	0.139	**1.26E-5**	0.704	0.196	**5.54E-6**	0.937	0.062	1.00
FLICM	4.149	3.100	*1.05E-1*	0.381	0.152	*1.87E-1*	0.759	0.162	**1.40E-5**	0.676	0.214	**2.36E-6**	**0.947**	0.050	1.00
sRFCM	**4.148**	3.099	-	**0.381**	0.152	-	**0.861**	0.054	-	**0.860**	0.073	-	0.867	0.097	-

TABLE II
COMPARATIVE PERFORMANCE ANALYSIS OF DIFFERENT SEGMENTATION ALGORITHMS ON BRAIN MR VOLUMES

Data Sets	Different Algorithms	Davies-Bouldin Index			Dunn Index			Dice Coefficient			Sensitivity			Specificity		
		Mean	Std Dev	p-value	Mean	Std Dev	p-value	Mean	Std Dev	p-value	Mean	Std Dev	p-value	Mean	Std Dev	p-value
BrainWeb (Noise-Bias)	FCM_S	0.168	0.064	**9.82E-5**	4.972	1.155	**9.82E-5**	0.904	0.023	**9.82E-5**	0.891	0.026	*1.33E-1*	0.980	0.004	**9.82E-5**
	FCM_S1	0.164	0.059	**9.82E-5**	5.134	1.045	**9.82E-5**	0.904	0.022	**9.82E-5**	0.891	0.026	*2.23E-1*	0.980	0.004	**9.82E-5**
	FCM_S2	0.161	0.059	**9.82E-5**	5.760	1.289	**1.17E-4**	0.905	0.022	**4.32E-4**	0.891	0.025	*2.10E-1*	0.981	0.004	**1.17E-4**
	KFCM_S	0.159	0.058	**9.82E-5**	4.963	1.406	**9.82E-5**	0.899	0.035	**9.82E-5**	0.887	0.036	**3.70E-3**	0.980	0.006	**1.17E-4**
	KFCM_S1	0.165	0.061	**9.82E-5**	4.965	1.048	**9.82E-5**	0.904	0.023	**9.82E-5**	0.892	0.026	*2.78E-1*	0.980	0.004	**9.82E-5**
	KFCM_S2	0.162	0.060	**9.82E-5**	5.684	1.324	**1.17E-4**	0.906	0.022	**7.96E-4**	0.891	0.026	*2.78E-1*	0.981	0.004	**9.82E-5**
	FLICM	0.230	0.077	**9.82E-5**	5.813	1.365	**1.17E-4**	0.868	0.012	**9.82E-5**	0.850	0.016	**9.82E-5**	0.978	0.003	**9.82E-5**
	KWFLICM	0.150	0.025	*1.98E-1*	4.945	0.864	**9.82E-5**	0.896	0.034	**9.82E-5**	0.883	0.036	**9.82E-5**	0.980	0.005	**9.82E-5**
	GHMRF	0.292	0.101	**9.82E-5**	3.772	0.618	**9.82E-5**	0.850	0.014	**9.82E-5**	0.829	0.016	**9.82E-5**	0.975	0.003	**9.82E-5**
	sRFCM	**0.143**	0.050	-	**7.109**	1.224	-	**0.910**	0.026	-	**0.893**	0.030	-	**0.981**	0.004	-
BrainWeb (Subject)	FCM_S	0.135	0.007	**4.43E-5**	3.442	0.544	**4.43E-5**	0.907	0.006	**4.43E-5**	0.906	0.012	1.00	0.988	0.002	**6.02E-5**
	FCM_S1	0.133	0.008	**4.43E-5**	3.528	0.557	**6.02E-5**	0.907	0.006	**4.43E-5**	0.906	0.012	1.00	0.988	0.002	**6.02E-5**
	FCM_S2	0.131	0.007	**4.43E-5**	3.774	0.583	**2.25E-4**	0.908	0.006	**1.41E-3**	0.905	0.012	9.99E-1	0.988	0.002	*1.66E-1*
	KFCM_S	0.129	0.008	**4.43E-5**	3.374	0.559	**4.43E-5**	0.907	0.006	**4.43E-5**	**0.906**	0.012	1.00	0.988	0.002	**4.43E-5**
	KFCM_S1	0.134	0.010	**4.43E-5**	3.401	0.571	**4.43E-5**	0.908	0.006	**4.43E-5**	0.906	0.012	1.00	0.988	0.002	**4.43E-5**
	KFCM_S2	0.131	0.007	**4.43E-5**	3.694	0.598	**1.95E-4**	0.908	0.006	**3.10E-2**	0.906	0.012	1.00	**0.988**	0.002	8.52E-1
	FLICM	0.220	0.016	**4.43E-5**	3.876	0.648	**2.28E-3**	0.883	0.008	**4.43E-5**	0.875	0.014	**4.43E-5**	0.987	0.002	**5.17E-5**
	KWFLICM	0.184	0.021	**5.17E-5**	2.632	0.574	**5.17E-5**	0.901	0.006	**4.43E-5**	0.899	0.012	**4.43E-5**	0.988	0.002	**5.17E-5**
	GHMRF	0.179	0.030	**5.17E-5**	2.517	0.782	**5.17E-5**	0.891	0.009	**4.43E-5**	0.889	0.016	**1.10E-4**	0.987	0.002	**4.43E-5**
	sRFCM	**0.115**	0.006	-	**4.206**	0.553	-	**0.909**	0.006	-	0.905	0.012	-	0.988	0.002	-
IBSR-18	FCM_S	0.265	0.041	**9.82E-5**	4.221	1.030	**1.17E-4**	0.765	0.033	**1.07E-3**	0.824	0.048	**1.64E-3**	0.981	0.009	**9.82E-5**
	FCM_S1	0.255	0.034	**9.82E-5**	4.437	1.093	**1.17E-4**	0.767	0.033	**1.24E-3**	0.825	0.048	**1.64E-3**	0.981	0.009	**9.82E-5**
	FCM_S2	0.239	0.035	**9.82E-5**	4.816	1.310	**1.17E-4**	0.774	0.033	**1.64E-3**	0.829	0.047	**3.70E-3**	0.982	0.009	**9.82E-5**
	KFCM_S	0.285	0.047	**9.82E-5**	3.664	0.809	**9.82E-5**	0.754	0.034	**5.88E-4**	0.819	0.049	**1.64E-3**	0.981	0.009	**9.82E-5**
	KFCM_S1	0.265	0.042	**9.82E-5**	4.209	1.087	**1.17E-4**	0.765	0.036	**1.07E-3**	0.823	0.050	**1.64E-3**	0.981	0.009	**9.82E-5**
	KFCM_S2	0.250	0.043	**9.82E-5**	4.551	1.315	**1.17E-4**	0.771	0.036	**1.43E-3**	0.827	0.049	**3.70E-3**	0.982	0.009	**1.17E-4**
	FLICM	0.226	0.018	**1.38E-4**	5.567	1.218	**9.82E-5**	0.785	0.055	**2.28E-4**	0.815	0.061	**9.82E-5**	0.983	0.010	**1.64E-4**
	KWFLICM	0.207	0.019	**3.15E-4**	5.297	1.403	**9.82E-5**	0.727	0.052	**9.82E-5**	0.793	0.059	**9.82E-5**	0.979	0.009	**9.82E-5**
	GHMRF	0.353	0.059	**9.82E-5**	3.520	0.948	**9.82E-5**	0.774	0.054	**9.82E-5**	0.806	0.062	**9.82E-5**	0.982	0.010	**9.82E-5**
	sRFCM	**0.174**	0.024	-	**7.946**	2.145	-	**0.804**	0.051	-	**0.834**	0.055	-	**0.983**	0.010	-
LPBA40	FCM_S	0.630	0.764	*1.80E-1*	2.332	1.192	**1.14E-7**	0.879	0.019	**4.34E-7**	0.922	0.018	**1.22E-4**	0.991	0.002	**3.78E-7**
	FCM_S1	0.633	0.768	*2.06E-1*	2.369	1.257	**4.41E-8**	0.880	0.018	**4.34E-7**	0.922	0.018	**1.15E-4**	0.991	0.002	**3.78E-7**
	FCM_S2	0.708	0.923	**1.28E-2**	2.524	1.312	**1.63E-7**	0.885	0.018	**8.55E-7**	**0.925**	0.017	**4.29E-4**	0.991	0.002	**4.05E-7**
	KFCM_S	0.834	0.738	**1.00E-2**	1.441	0.884	**5.50E-8**	0.840	0.056	**1.78E-8**	0.893	0.050	**2.81E-8**	0.989	0.003	**1.78E-8**
	KFCM_S1	0.939	0.768	**4.72E-4**	1.051	0.547	**4.75E-8**	0.827	0.052	**1.78E-8**	0.887	0.050	**3.27E-8**	0.988	0.003	**1.78E-8**
	KFCM_S2	0.889	0.771	**2.93E-3**	1.226	0.706	**5.11E-8**	0.840	0.057	**1.78E-8**	0.895	0.053	**5.50E-8**	0.989	0.003	**1.78E-8**
	FLICM	0.663	0.786	**6.21E-3**	2.579	1.387	**5.70E-7**	0.842	0.051	**1.78E-8**	0.867	0.027	**1.93E-8**	0.989	0.003	**1.78E-8**
	KWFLICM	**0.601**	0.774	*1.16E-1*	2.822	1.652	**9.02E-6**	0.866	0.032	**3.29E-7**	0.916	0.028	**1.54E-5**	0.990	0.003	**2.86E-7**
	GHMRF	0.654	0.577	*5.64E-2*	2.010	1.036	**8.54E-8**	0.824	0.048	**1.78E-8**	0.851	0.034	**1.78E-8**	0.988	0.003	**1.78E-8**
	sRFCM	0.682	0.923	-	**3.648**	2.366	-	**0.899**	0.040	-	0.924	0.039	-	**0.992**	0.002	-

Finally, the qualitative comparative results are reported in Fig. 5 on some HEp-2 cell images and in Figs. 6 and 7 on some brain MR volumes for some of the methods as examples. In case of brain tissue segmentation, the proposed and some existing algorithms, namely, FCM_S, KFCM_S, FLICM, and KWFLICM, are applied on bias corrected and skull stripped brain MR volumes. Other three MRI analysis tools, namely, FSL, SPM, and volBrain, are given original inputs, instead of preprocessed one, since they have their own skull stripping and bias correction mechanisms. Therefore, preprocessed volumes of column (b) of Figs. 6 and 7 serve as input for segmentation results of columns (d)–(h), whereas original brain MR volumes of column (a) act as input for the results of MRI tools presented in columns (i)–(k) of Figs. 6 and 7. The segmented images in Figs. 6 and 7 are taken from middle slices of three views, namely, axial, coronal, and sagittal, for each MR volume. The segmented images obtained using different algorithms establish the fact that the output images generated by the sRFCM algorithm is

Authorized licensed use limited to: Indian Statistical Institute Kolkata. Downloaded on May 08,2020 at 03:48:34 UTC from IEEE Xplore. Restrictions apply.

TABLE III
COMPARATIVE PERFORMANCE ANALYSIS OF SRFCM AND DIFFERENT BRAIN MR VOLUME ANALYSIS TOOLS

Data Sets	Different Algorithms	Dice Coefficient			Sensitivity			Specificity		
		Mean	Std Dev	p-value	Mean	Std Dev	p-value	Mean	Std Dev	p-value
BrainWeb (Noise-Bias)	FSL	0.870	0.016	**9.82E-5**	0.866	0.016	**9.82E-5**	0.977	0.003	**9.82E-5**
	SPM	0.849	0.028	**9.82E-5**	**0.923**	0.023	9.99E-1	0.978	0.005	**4.21E-3**
	volBrain	0.904	0.004	*9.20E-2*	0.883	0.003	*9.20E-2*	0.981	0.001	*2.93E-1*
	sRFCM	**0.910**	0.026	-	0.893	0.030	-	**0.981**	0.004	-
BrainWeb (Subject)	FSL	0.898	0.006	**4.43E-5**	0.909	0.013	1.00	0.988	0.002	**1.52E-2**
	SPM	0.863	0.012	**4.43E-5**	**0.931**	0.004	1.00	0.988	0.001	*2.06E-1*
	volBrain	0.890	0.007	**4.43E-5**	0.872	0.010	**4.43E-5**	0.983	0.002	**4.43E-5**
	sRFCM	**0.909**	0.006	-	0.905	0.012	-	**0.988**	0.002	-
IBSR-18	FSL	0.764	0.024	**1.64E-3**	0.828	0.050	**8.81E-3**	0.982	0.007	**2.48E-3**
	SPM	0.733	0.020	**1.13E-3**	**0.875**	0.018	9.99E-1	0.983	0.004	*3.26E-1*
	volBrain	0.799	0.026	*9.94E-2*	0.809	0.032	**2.91E-2**	**0.985**	0.003	6.92E-1
	sRFCM	**0.804**	0.051	-	0.834	0.055	-	0.983	0.010	-
LPBA40	FSL	0.860	0.016	**3.29E-7**	0.916	0.018	**1.02E-5**	0.990	0.002	**2.49E-7**
	SPM	0.790	0.019	**2.61E-8**	0.902	0.030	**4.97E-7**	0.983	0.002	**1.78E-8**
	volBrain	0.714	0.070	**1.93E-8**	0.700	0.081	**1.93E-8**	0.948	0.029	**1.78E-8**
	sRFCM	**0.899**	0.040	-	**0.924**	0.039	-	**0.992**	0.002	-

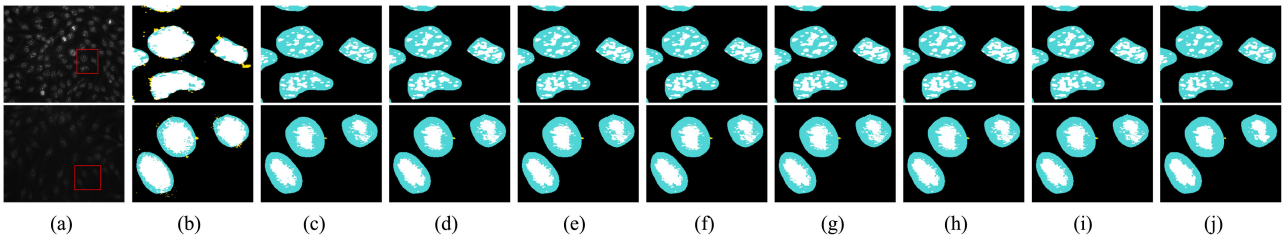

Fig. 5. Input and segmented images of HEp-2 cell obtained using different algorithms for image no. 03 and 20 (top to bottom). The white, yellow and blue colors, in segmented images, represent true positive, false positive and false negative regions, respectively. (a) Input. (b) sRFCM. (c) Otsu. (d) FCM_S. (e) FCM_S1. (f) FCM_S2. (g) KFCM_S. (h) KFCM_S1. (i) KFCM_S2. (j) FLICM.

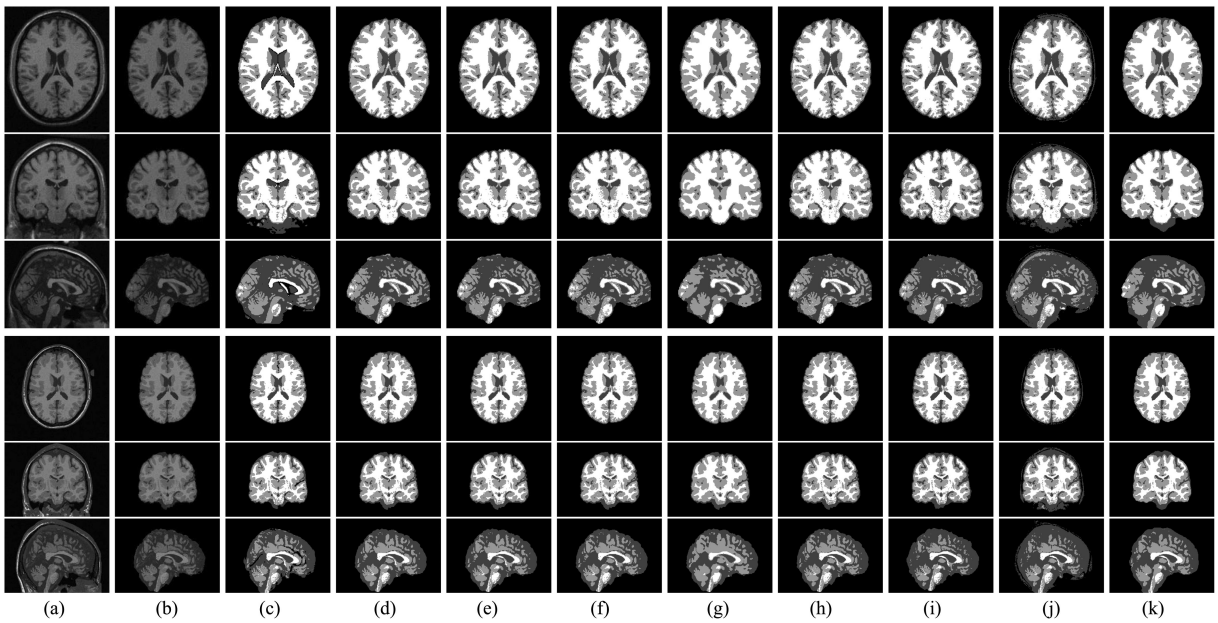

Fig. 6. Original, preprocessed, reference, and segmented images of BrainWeb using different algorithms (top: Noise-Bias: 5%–40%; bottom: subject 18). (a) Original. (b) Preprocessed. (c) Reference. (d) sRFCM. (e) FCM_S. (f) KFCM_S. (g) FLICM. (h) KWFLICM. (i) FSL. (j) SPM. (k) volBrain.

more promising than that obtained using existing segmentation methods. The best performance of the proposed method is achieved due to the fact that spatial constraint incorporated in the sRFCM balances the robustness to both added noise and outliers, and effectiveness of preserving the details for image. Moreover, the overlapping partitions are handled efficiently by the probabilistic membership function of the sRFCM, while the arbitrary shaped core region of a cluster can be identified by the possibilistic membership function of lower approximation. Also, the concept of core and boundary regions of a cluster,

Authorized licensed use limited to: Indian Statistical Institute Kolkata. Downloaded on May 08,2020 at 03:48:34 UTC from IEEE Xplore. Restrictions apply.

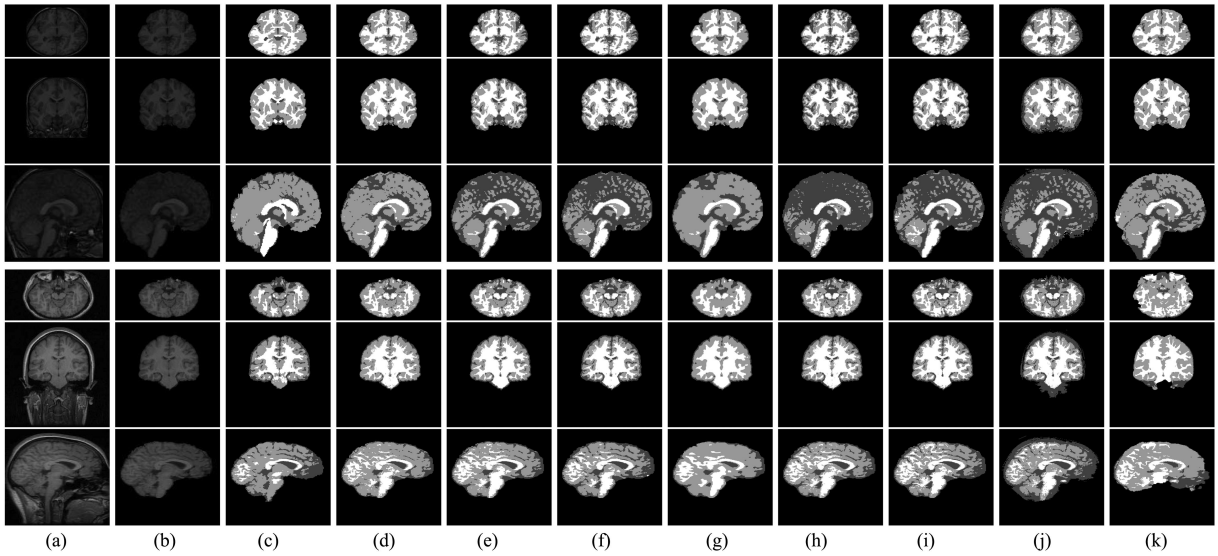

Fig. 7. Original, preprocessed, reference, and segmented images of IBSR-18 (top: vol 14) and LPBA40 (bottom: vol S25) obtained using different algorithms. (a) Original. (b) Preprocessed. (c) Reference. (d) sRFCM. (e) FCM_S. (f) KFCM_S. (g) FLICM. (h) KWFLICM. (i) FSL. (j) SPM. (k) volBrain.

introduced in the sRFCM, can deal with uncertainty, vagueness, and incompleteness in segment definition. In effect, the proposed image segmentation algorithm can generate good segmented regions.

IV. Conclusion

The contribution of the article lies in developing a new clustering algorithm, termed as sRFCM, for segmentation of medical images. It judiciously integrates the merits of rough-fuzzy clustering and local spatial constraint of each pixel. The spatial constraint of the proposed sRFCM algorithm permits the labeling of a pixel to be persuaded by the labels of its neighboring pixels. Hence, the proposed sRFCM algorithm can avoid the problem of sensitivity to imaging artifacts of existing rough-fuzzy clustering algorithms. The spatial constraint is used to balance between the robustness to both added noise and outliers, and effectiveness of preserving the image details. Moreover, the notion of core and boundary regions of rough sets, used in the sRFCM algorithm, deals with incompleteness in cluster definition, while both possibilistic and probabilistic membership functions of fuzzy sets enable efficient handling of overlapping partitions in noisy environment. The proposed parameter optimization technique is found to be effective in determining optimum values of neighborhood regularizer and weight parameter. Finally, the effectiveness of the proposed sRFCM algorithm is demonstrated on brain MR and HEp-2 cell image segmentation, along with a comparison with other application-dependent existing algorithms.

Acknowledgment

This article is an outcome of the R&D work undertaken in the project under the Visvesvaraya PhD Scheme of Ministry of Electronics and Information Technology, Government of India, being implemented by Digital India Corporation.

References

[1] B. Vasilic and F. W. Wehrli, "A novel local thresholding algorithm for trabecular bone volume fraction mapping in the limited spatial resolution regime of in vivo MRI," *IEEE Trans. Med. Imag.*, vol. 24, no. 12, pp. 1574–1585, Dec. 2005.

[2] J. C. Bezdek, L. O. Hall, and L. P. Clarke, "Review of MR image segmentation techniques using pattern recognition," *Med. Phys.*, vol. 20, no. 4, pp. 1033–1048, 1993.

[3] N. Otsu, "A threshold selection method from gray level histogram," *IEEE Trans. Syst., Man, Cybern.*, vol. SMC-9, no. 1, pp. 62–66, Jan. 1979.

[4] H. D. Li, M. Kallergi, L. P. Clarke, V. K. Jain, and R. A. Clark, "Markov random field for tumor detection in digital mammography," *IEEE Trans. Med. Imag.*, vol. 14, no. 3, pp. 565–576, Sep. 1995.

[5] C. Lee, S. Huh, T. Ketter, and M. Unser, "Unsupervised connectivity-based thresholding segmentation of midsagittal brain MR images," *Comput. Biol. Med.*, vol. 28, no. 3, pp. 309–338, 1998.

[6] I. Levner and H. Zhang, "Classification-driven watershed segmentation," *IEEE Trans. Image Process.*, vol. 16, no. 5, pp. 1437–1445, May 2007.

[7] A. K. Qin and D. A. Clausi, "Multivariate image segmentation using semantic region growing with adaptive edge penalty," *IEEE Trans. Image Process.*, vol. 19, no. 8, pp. 2157–2170, Aug. 2010.

[8] L. Zhu, Y. Gao, A. Yezzi, and A. Tannenbaum, "Automatic segmentation of the left atrium from MR images via variational region growing with a moments-based shape prior," *IEEE Trans. Image Process.*, vol. 22, no. 12, pp. 5111–5122, Dec. 2013.

[9] J. F. Mangin, V. Frouin, I. Bloch, J. Rgis, and J. Lpez-Krahe, "From 3D magnetic resonance images to structural representations of the cortex topography using topology preserving deformations," *J. Math. Imag. Vision*, vol. 5, no. 4, pp. 297–318, 1995.

[10] L. O. Hall, A. M. Bensaid, L. P. Clarke, R. P. Velthuizen, M. S. Silbiger, and J. C. Bezdek, "A comparison of neural network and fuzzy clustering techniques in segmenting magnetic resonance images of the brain," *IEEE Trans. Neural Netw.*, vol. 3, no. 5, pp. 672–682, Sep. 1992.

[11] W. E. Reddick, J. O. Glass, E. N. Cook, T. D. Elkin, and R. J. Deaton, "Automated segmentation and classification of multispectral magnetic resonance images of brain using artificial neural networks," *IEEE Trans. Med. Imag.*, vol. 16, no. 6, pp. 911–918, Dec. 1997.

[12] J. Zhang, Q. Liu, and Z. Chen, "A medical image segmentation method based on SOM and wavelet transforms," *J. Commun. Comput.*, vol. 2, no. 5, pp. 46–50, 2005.

[13] T. McInerney and D. Terzopoulos, "T-snakes: Topology adaptive snakes," *Med. Image Anal.*, vol. 4, no. 2, pp. 73–91, 2000.

[14] G. Kühne, J. Weickert, M. Beier, and W. Effelsberg, *Fast Implicit Active Contour Models*. Berlin, Germany: Springer, 2002, pp. 133–140.

[15] G. N. Abras and V. L. Ballarin, "A weighted K-means algorithm applied to brain tissue classification," *J. Comput. Sci. Technol.*, vol. 5, no. 3, pp. 121–126, 2005.

Authorized licensed use limited to: Indian Statistical Institute Kolkata. Downloaded on May 08,2020 at 03:48:34 UTC from IEEE Xplore. Restrictions apply.

[16] B. Vemuri, S. Rahman, and J. Li, "Multiresolution adaptive K-means algorithm for segmentation of brain MRI," *Image Anal. Appl. Comput. Graph.*, vol. 1024, pp. 347–354, 1995.
[17] P. Maji and S. Roy, "Rough-fuzzy clustering and unsupervised feature selection for wavelet based MR image segmentation," *PLoS One*, vol. 10, no. 4, 2015, Art. no. e0123677.
[18] L. Chen, Q. Jiang, and S. Wang, "Model-based method for projective clustering," *IEEE Trans. Knowl. Data Eng.*, vol. 24, no. 7, pp. 1291–1305, Jul. 2012.
[19] Y. Li and Z. Chi, "MR brain image segmentation based on self-organizing map network," *Int. J. Inf. Technol.*, vol. 11, no. 8, pp. 45–53, 2005.
[20] M. E. Brandt, T. P. Bohan, L. A. Kramer, and J. M. Fletcher, "Estimation of CSF, white and gray matter volumes in hydrocephalic children using fuzzy clustering of MR images," *Comput. Med. Imag. Graph.*, vol. 18, pp. 25–34, 1994.
[21] C. L. Li, D. B. Goldgof, and L. O. Hall, "Knowledge-based classification and tissue labeling of MR images of human brain," *IEEE Trans. Med. Imag.*, vol. 12, no. 4, pp. 740–750, Dec. 1993.
[22] Z. Liang, J. R. MacFall, and D. P. Harrington, "Parameter estimation and tissue segmentation from multispectral MR images," *IEEE Trans. Med. Imag.*, vol. 13, no. 3, pp. 441–449, Sep. 1994.
[23] T. M. Nguyen and Q. M. J. Wu, "Fast and robust spatially constrained gaussian mixture model for image segmentation," *IEEE Trans. Circuits Syst. for Video Technol.*, vol. 23, no. 4, pp. 621–635, Apr. 2013.
[24] P. Maji and S. K. Pal, "Rough set based generalized fuzzy c-means algorithm and quantitative indices," *IEEE Trans. System, Man, Cybern. B, Cybern.*, vol. 37, no. 6, pp. 1529–1540, Dec. 2007.
[25] P. Maji and S. Paul, "Rough-fuzzy clustering for grouping functionally similar genes from microarray data," *IEEE/ACM Trans. Comput. Biol. Bioinf.*, vol. 10, no. 2, pp. 286–299, Mar./Apr. 2013.
[26] P. Maji and S. K. Pal, *Rough-Fuzzy Pattern Recognition: Applications in Bioinformatics and Medical Imaging*. Hoboken, NJ, USA: Wiley, 2012.
[27] Y. Zhang, M. Brady, and S. Smith, "Segmentation of brain MR images through a hidden Markov random field model and the expectation-maximization algorithm," *IEEE Trans. Med. Imag.*, vol. 20, no. 1, pp. 45–57, Jan. 2001.
[28] D. L. Pham and J. L. Prince, "Adaptive fuzzy segmentation of magnetic resonance images," *IEEE Trans. Med. Imag.*, vol. 18, no. 9, pp. 737–752, Sep. 1999.
[29] M. N. Ahmed, S. M. Yamany, N. Mohamed, A. A. Farag, and T. Moriarty, "A modified fuzzy c-means algorithm for bias field estimation and segmentation of MRI data," *IEEE Trans. Med. Imag.*, vol. 21, no. 3, pp. 193–199, Mar. 2002.
[30] H. Zhang, Q. M. J. Wu, and T. M. Nguyen, "A robust fuzzy algorithm based on student's t-distribution and mean template for image segmentation application," *IEEE Signal Process. Lett.*, vol. 20, no. 2, pp. 117–120, Feb. 2013.
[31] M. Gong, Y. Liang, J. Shi, W. Ma, and J. Ma, "Fuzzy c-means clustering with local information and kernel metric for image segmentation," *IEEE Trans. Image Process.*, vol. 22, no. 2, pp. 573–584, Feb. 2013.
[32] W. Cai, S. Chen, and D. Zhang, "Fast and robust fuzzy c-means clustering algorithms incorporating local information for image segmentation," *Pattern Recognit.*, vol. 40, pp. 825–838, 2007.
[33] Y. Xia, D. Feng, T. Wang, R. Zhao, and Y. Zhang, "Image segmentation by clustering of spatial patterns," *Pattern Recognit. Lett.*, vol. 28, pp. 1548–1555, 2007.
[34] X.-Y. Wang and J. Bu, "A fast and robust image segmentation using FCM with spatial information," *Digit. Signal Process.*, vol. 20, pp. 1173–1182, 2010.
[35] Z. Yang, F.-L. Chung, and W. Shitong, "Robust fuzzy clustering-based image segmentation," *Appl. Soft Comput.*, vol. 9, pp. 80–84, 2009.
[36] S. Chen and D. Zhang, "Robust image segmentation using FCM with spatial constraints based on new kernel-induced distance measure," *IEEE Trans. Syst., Man, Cybern. B, Cybern.*, vol. 34, no. 4, pp. 1907–1916, Aug. 2004.
[37] S. Krinidis and V. Chatzis, "A robust fuzzy local information c-means clustering algorithm," *IEEE Trans. Image Process.*, vol. 19, no. 5, pp. 1328–1337, May 2010.
[38] A. W.-C. Liew and H. Yan, "An adaptive spatial fuzzy clustering algorithm for 3-D MR image segmentation," *IEEE Trans. Med. Imag.*, vol. 22, no. 9, pp. 1063–1075, Sep. 2003.
[39] Y. A. Tolias and S. M. Panas, "Image segmentation by a fuzzy clustering algorithm using adaptive spatially constrained membership functions," *IEEE Trans. Syst., Man, Cybern. A, Syst., Humans*, vol. 28, no. 3, pp. 359–369, May 1998.
[40] J. Liu and T. D. Pham, "A spatially constrained fuzzy hyper-prototype clustering algorithm," *Pattern Recognit.*, vol. 45, pp. 1759–1771, 2012.
[41] L. Wan, T. Zhang, Y. Xiang, and H. You, "A robust fuzzy c-means algorithm based on bayesian nonlocal spatial information for SAR image segmentation," *IEEE J. Sel. Topics Appl. Earth Observ. Remote Sens.*, vol. 11, no. 3, pp. 896–906, Mar. 2018.
[42] C. Wu and Y. Chen, "Adaptive entropy weighted picture fuzzy clustering algorithm with spatial information for image segmentation," *Appl. Soft Comput.*, vol. 86, 2019, Art. no. 105888.
[43] Y. Zhang, X. Bai, R. Fan, and Z. Wang, "Deviation-sparse fuzzy c-means with neighbor information constraint," *IEEE Trans. Fuzzy Syst.*, vol. 27, no. 1, pp. 185–199, Jan. 2019.
[44] J. Dolz, C. Desrosiers, and I. B. Ayed, "3D fully convolutional networks for subcortical segmentation in MRI: A large-scale study," *NeuroImage*, vol. 170, pp. 456–470, 2018.
[45] G. James, *Modern Engineering Mathematics*. Reading, MA, USA: Addison-Wesley, 1996.
[46] J. Bezdek, R. J. Hathaway, M. J. Sabin, and W. T. Tucker, "Convergence theory for fuzzy c-means: Counterexamples and repairs," *IEEE Trans. Syst., Man, Cybern.*, vol. SMC-17, no. 5, pp. 873–877, Sep./Oct. 1987.
[47] J. V. Manjon and P. Coupe, "volBrain: An online MRI brain volumetry system," *Frontiers Neuroinformatics*, vol. 10, p. 30, 2016.
[48] M. Jenkinson, C. F. Beckmann, T. E. Behrens, M. W. Woolrich, and S. M. Smith, "FSL," *NeuroImage*, vol. 62, no. 2, pp. 782–790, 2012.
[49] J. Ashburner and K. J. Friston, "Unified segmentation," *NeuroImage*, vol. 26, no. 3, pp. 839–851, 2005.
[50] P. Foggia, G. Percannella, P. Soda, and M. Vento, "Benchmarking HEp-2 cells classification methods," *IEEE Trans. Med. Imag.*, vol. 32, no. 10, pp. 1878–1889, Oct. 2013.
[51] B. Aubert-Broche, M. Griffin, G. B. Pike, A. C. Evans, and D. L. Collins, "Twenty new digital brain phantoms for creation of validation image data bases," *IEEE Trans. Med. Imag.*, vol. 25, no. 11, pp. 1410–1416, Nov. 2006.
[52] C. A. Cocosco, V. Kollokian, R. K.-S. Kwan, G. B. Pike, and A. C. Evans, "BrainWeb: Online interface to a 3D MRI simulated brain database," *NeuroImage*, vol. 5, p. 425, 1997.
[53] D. W. Shattuck *et al.*, "Construction of a 3D probabilistic atlas of human cortical structures," *NeuroImage*, vol. 39, no. 3, pp. 1064–1080, 2008.
[54] S. M. Smith, "Fast robust automated brain extraction," *Human Brain Mapping*, vol. 17, pp. 143–155, 2002.
[55] N. J. Tustison *et al.*, "N4ITK: Improved N3 bias correction," *IEEE Trans. Med. Imag.*, vol. 29, no. 6, pp. 1310–1320, Jun. 2010.

Shaswati Roy received the B.Tech degree in information technology from the West Bengal University of Technology, Kolkata, India, in 2005, and M.E. degree in information technology from Jadavpur University, Kolkata, in 2012.

Currently, she is a Research Scholar with the Machine Intelligence Unit, Indian Statistical Institute, Kolkata. She has authored or coauthored a few papers in international journals and conferences. Her research interests include medical image processing, machine learning, soft computing, and so forth.

Ms. Roy has received the prestigious INSPIRE fellowship of the Department of Science and Technology, Government of India for the years 2015–2020.

Pradipta Maji received the B.Sc. degree in physics, the M.Sc. degree in electronics science, and the Ph.D. degree in the area of computer science from Jadavpur University, Kolkata, India, in 1998, 2000, and 2005, respectively.

Currently, he is a Professor with the Machine Intelligence Unit, Indian Statistical Institute, Kolkata, India. He has authored or coauthored more than 125 papers in international journals and conferences. His research interests include pattern recognition, machine learning, computational biology and bioinformatics, medical image processing, and so forth.

Dr. Maji is a Fellow of the National Academy of Sciences, India. He has received the 2008 Microsoft Young Faculty Award from Microsoft Research Laboratory India Pvt., the 2009 Young Scientist Award from the National Academy of Sciences, India, the 2011 Young Scientist Award from the Indian National Science Academy, India, and the 2015 Young Faculty Research Fellowship from the Ministry of Electronics and Information Technology, Government of India. He has been selected as the 2009 Young Associate of the Indian Academy of Sciences, India.

Authorized licensed use limited to: Indian Statistical Institute Kolkata. Downloaded on May 08,2020 at 03:48:34 UTC from IEEE Xplore. Restrictions apply.